Inverse Problems **10** (1994) 185–197. Printed in the UK

# Thermal-wave slice tomography using wave-field reconstruction

O Padé† and A Mandelis

Photothermal and Optoelectronic Diagnostics Laboratory, Department of Mechanical Engineering, University of Toronto, Toronto, Ontario M5S 1A4, Canada

Received 29 June 1992, in final form 6 August 1993

**Abstract.** A new matrix-equation-based theoretical computation method for detection of subsurface defects by thermal-wave tomographic imaging is presented. The method uses the measured scattered temperature field to solve the Helmholtz thermal pseudowave equation, by solving the equivalent integral equation. Numerical results are presented and compared with the ray optic calculation. The numerical calculations of the inverse problem were carried out using the Born approximation, however the theoretical technique is capable of handling the general tomographic inverse case without recourse to the Born approximation.

## 1. Introduction

Thermal-wave imaging as a method of detecting subsurface defects has been the subject of intensive study in recent years [1–8]. However, most of the research was either purely theoretical [3, 4] or experimental which used simple methods of reconstruction [5–7].

Unlike electromagnetic or acoustic tomography, thermal-wave tomography suffers from the facts that propagation distances of the thermal wave are short, and the wave number is complex, which means that the wave is strongly damped and thus the sample cannot be rotated [5]. Therefore the regular tomographic reconstructions [9] are not applicable to the thermal wave problem.

A one-dimensional ray-optic-based reconstruction technique was described previously [5], and was quite successful in illustrating the principle for obtaining thermal diffusivity images of spatial cross sections perpendicular to the photothermally excited surface (thermal-wave slice tomograms, analogous in their definition to acoustic/ultrasonic tomograms as described by Kak and Slaney [9]). However, using only ray-optic methods has many limitations, especially in highly dispersive wave fields, such as thermal waves. For this reason techniques familiar from x-ray cross sectional tomography, such as recovery of a 2D image from an over sampled 1D projection, cannot be applied to thermal wave tomography with satisfactory image contrast, resolution and low distortion. Layer, time-slice, non-multiplexing techniques were described by Favro *et al* [7]. These workers were able to reconstruct the shape of the subsurface inhomogeneities, but not to accurately determine their depth, using a technique akin to the one based on the photothermal impulse response method [10]. Some work on backscattering of thermal waves is described in [8]. Other imaging

† On leave from Rafael, PO Box 2250, Haifa 31021, Israel.

0266-5611/94/010185 + 13$07.50  

methods are described in [1, 2]. In this paper we describe a new rigorous reconstruction method based on the solution of the thermal Helmholtz pseudo-wave equation. We calculate Green's function for the equation and then using the Born approximation we reconstruct the thermal diffusivity of the examined sample. The method is further capable of solving the Helmholtz equation without the assumption of the Born approximation. However, at this stage of the research we shall present the simpler reconstructions using the Born approximation.

## 2. Mathematical background

In the case of a harmonic photothermal excitation of a region of space, the temperature oscillation is found to obey the Helmholtz pseudowave equation [3, 4]:

$$[\nabla^2 + \tilde{k}^2(r)]T(r) = 0 \tag{1}$$

where

$$\tilde{k}(r) = (1 - \mathrm{i})\left[\frac{\omega}{2\alpha(r)}\right]^{1/2} \tag{2}$$

$\alpha(r)$ is the thermal diffusivity and $\omega$ is the angular frequency of the modulation of the laser beam intensity, typically in the 1–1000 Hz range for a thermal wave experiment. The actual value of $\omega$ in a given experimental case depends on the depth in the material to be probed. $|\tilde{k}|$ represents the inverse of the RMS depth probed thermally by the technique (the so-called 'thermal diffusion length'). $\tilde{k}(r)$ is the complex thermal wavenumber. In a metal such as aluminium typical values of $|\tilde{k}| = (2\pi f/\alpha)^{1/2}$ are 2.7–87.5 $\mathrm{cm}^{-1}$ in the above mentioned modulation frequency range ($\alpha = 0.82\,\mathrm{cm}^2\,\mathrm{s}^{-1}$ [11]). For thermal insulators this range of $|\tilde{k}|$ values increases substantially. In all physical cases, however, thermal-wave $|\tilde{k}|$ values remain much lower than comparable acoustic (ultrasonic) or optical wavenumber ranges. It was found that to be consistent with the experimental results, the thermal excitation should be described by the law: $T = T_0\,\mathrm{e}^{\mathrm{i}\omega t}$. This sign selection of the exponent is important here, in contrast with the conventional optical excitation, where the sign of the exponent is irrelevant due to the use of the second derivative with respect to time.

Upon defining [4]

$$F(r) = \begin{cases} \tilde{k}_0^2[\nu^2(r) - 1] & r \in R \\ 0 & r \notin R \end{cases} \tag{3}$$

the starting equation for the thermal-wave tomographic problem is the diffusion (Helmholtz pseudowave) equation which takes the form [3]

$$(\nabla^2 + \tilde{k}_0^2)T(r) = -F(r)T(r). \tag{4}$$

In equation (3) we defined

$$\nu(r) \equiv [\alpha_0/\alpha(r)]^{1/2} \tag{5}$$

and

$$\tilde{k}_0 = (1 - \mathrm{i})\left(\frac{\omega}{2\alpha_0}\right)^{1/2} \equiv k_0 \, \mathrm{e}^{-\mathrm{i}\pi/4} \tag{6}$$

$\alpha_0$ is the diffusivity of the homogeneous (reference) region surrounding the object region $R$. The AC (thermal-wave) temperature field at angular frequency $\omega$, i.e. the solution of equation (4) satisfies in three dimensions [9],

$$T(r) = T_i(r) + \iiint G_0(r|\rho)F(\rho)T(\rho)\,\mathrm{d}^3\rho \tag{7}$$

where $T(r)$ represents the entire thermal-wave field (incident and scattered) oscillating at $f = \omega/2\pi$. the integration is carried over the spatial object region $R$. In this work we assume that the region $R$ is a slice in 2D space [4]. Moreover, we assume that $R$ is rectangular where the thermal excitation is on one side of the region ($y = 0$), and the detection is on the other side ($y = l = y_f$ (figure 1)).

If the thermal-wave field $T(x, y = y_f)$ is measured, and if

$$T(r) = T_i(r) + T_s(r) \tag{8}$$

then using equation (4) we obtain

$$T_s(x, y_f) = \int_{x_i}^{x_f} \int_0^{y_f} G_0[r(x, y_f)|\rho(\xi, \eta)]F[\rho(\xi, \eta)]T[\rho(\xi, \eta)]\,\mathrm{d}\xi\,\mathrm{d}\eta \tag{9}$$

$G_0$ is the Greens function for the region $R$, with the property

$$G_0(r|\rho) = G_0(|r - \rho|). \tag{10}$$

Relation (10) is justified if the distance between the boundary $S$ which encloses the spatial region $R$ and the thermal-wave source point $\rho$ and/or the observation point $r$, is not small compared with the magnitude of $\rho$ and/or $r$ [12].

The conventional techniques used in electromagnetic or acoustic tomography for solving integral equations of the type of equation (9) are by Fourier transform methods [9]. Usually one obtains the one-dimensional Fourier transform of $T_s$ for every position of the exciting laser, and by using the Fourier slice theorem [9] it is possible to obtain a map of the inhomogeneity of the object. When thermal waves are involved we have complex wavenumber, short paths of propagation of the waves leading to the extreme near field approximation [3], and the requirement for a generalized two-dimensional spatial Laplace transform inversion [4], a non-trivial task. Furthermore the fact that the movements of the laser and the detector aperture are limited to straight lines make it necessary to utilize other methods for solving equation (9). The ultrasonic experimental geometry in [13] is similar to the one described in figure 1. However the method described in [13] uses only real values for $\tilde{k}_0$ in order to avoid inversion of Laplace transforms, a situation which is unavoidable with thermal waves.

### 3. The computational method for the inverse problem

The proposed technique is based on a special method of discretization of equation (8). The edge of the sampled region ($y = y_f$) is divided into $n^2$ intervals, and in the

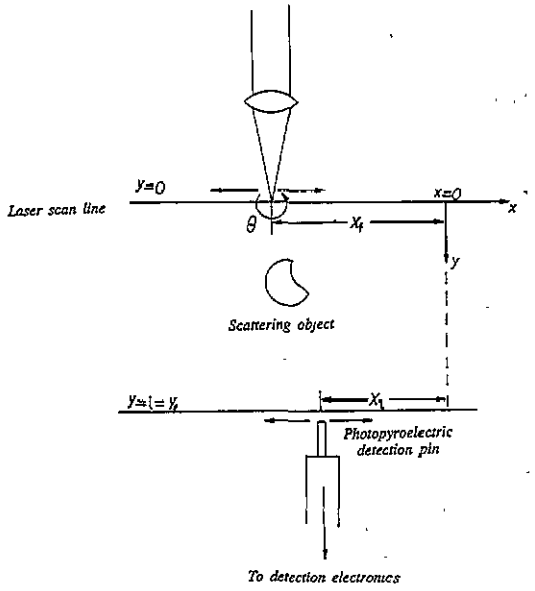


**Figure 1.** Geometry for synthetic aperature photothermal-wave diffraction tomography using scanning thin film pyroelectric detection. For each position of the laser beam waist on the line $y = 0$, the metal pin detector measures the thermal-wave field characteristics (amplitude and phase) along the back surface $y = l$ line.

rectangular region

$$R = \{(x, y)|x_i \leq x \leq x_f; 0 \leq y \leq y_f\} \tag{11}$$

we choose $n^2$ points. The idea to use $n^2$ points in the boundary is essential for obtaining a square matrix. The '$n^2$' comes from the fact that the integral in equation (12) below is a double integral, which will be discretized in equation (14).

Now, for $1 \leq j \leq n^2$, equation (9) assumes the following form

$$T_s(j\Delta x, y_f) = \int_{x_i}^{x_f} \int_0^{y_f} G_0[r(j\Delta x, y_f)|\rho(\xi, \eta)]T[\rho(\xi, \eta)]\,\mathrm{d}\xi\,\mathrm{d}\eta. \tag{12}$$

We order the grid points in $R$, $(k\Delta\xi, l\Delta\eta)$ in the following matrix order $m(k, l)$:

$$\begin{pmatrix} 1 & 2 & 6 & 7 & 15 & 16 & \cdot \\ 3 & 5 & 8 & 14 & 17 & \cdot & \\ 4 & 9 & 13 & 18 & \cdot & & \\ 10 & 12 & 19 & \cdot & & & \\ 11 & 20 & \cdot & & & & \\ 21 & \cdot & & & & & \\ \cdot & & & & & & \end{pmatrix}. \tag{13}$$

The type of order is quite general. We chose the order in matrix (13) because it is not dependent on the matrix dimension and hence is more general than ordering which is dependent on the dimension of the matrix. Moreover this ordering is not difficult for programming.

Discretizing equation (12), we obtain

$$T_s(k\Delta x, y_f) = \sum_{m=1}^{n^2} G_0(|r_k - \rho_m|)F(\rho_m)T(\rho_m) \tag{14}$$

where

$$\rho_m = \rho_{m(i,j)} = \langle (i\Delta\xi)^2, (j\Delta\eta)^2 \rangle \tag{15}$$

and the right-hand side of equation (15) indicates the norm of a vector with grid components $i\Delta\zeta$ and $j\Delta\eta$ measured from the origin. Formally the left-hand side of equation (14) is known from the photothermal tomographic measurement [5], whereas calculation of Green's function for the present problem is carried out in appendix A. Therefore the linear system (14) can be solved for the multiplicity $FT$, which is the object function $F$ multiplied by the temperature field $T$. At this stage we have the value of $FT$ in the entire region $R$, so now we can calculate the scattered field in the entire region $R$, by

$$T_s(k\Delta x, l\Delta y) = \sum_{i=1}^{n}\sum_{j=1}^{n} G_0(|r_{k,l} - \rho_{m(i,j)}|)F(\rho_{m(i,j)})T(\rho_{m(i,j)}). \tag{16}$$

Carrying out the double sum (16) for $0 \le k,\ l \le n$ results in obtaining the scattered field $T_s$ in the entire cross-sectional region. The use of a $n^2 \times n^2$ matrix requires considerable computer resources. However, in the current state of computer development it is not a severe restriction. For example, the solution of equation (16) for $n = 25$, which means a system of 625 equations with 625 unknowns, takes about an hour on a Sun4 workstation, and would take (without vectorization) about 300 seconds on a Convex computer. Thus using equation (8) the thermal-wave field is known, and it is easy now to calculate $F$ and to obtain the behaviour of the thermal diffusivity and hence the inhomogeneities of the sample.

In this work we use only the first Born approximation [9], namely, in equation (12) we use $T_i$ instead of $T$. $T_i$ is known (see appendix B) and we solve equation (14) directly for $F$. The Born approximation is used because it simplifies the computations, and it demands less time than the full solution. The present paper shows the feasibility of the Born method which provides satisfactory inversions in the range of our simulation and experimental parameters. The method of complete recovery of $T$ is currently under numerical computer implementation.

Defining a matrix of coefficients $A$ by

$$A_{km} = G_0(|r_k - \rho_m|) \tag{17}$$

we have the following $n^2 \times n^2$ system of linear equations

$$Af = t \tag{18}$$

where $f = FT$ and $t = T_s$.

The main problem with this method, from the computational point of view, is that the matrix $G_0T_i$ is in many cases almost singular. To overcome this problem we can use either the Tykhonov regularization method or we solve the system using SVD (singular value decomposition) [14]. In this work we mainly use the Tykhonov regularization [15, 16], which means that we have to minimize the functional,

$$\phi(z) = \|Az - t\|_2 + \sigma\Omega(z) \tag{19}$$

where $\Omega(z)$ is a positive convex functional [16]. For reasons of simplicity and ease of computation, we chose $\Omega(z)$ to be

$$\Omega(z) = \|z\|_2 = \sqrt{\sum_{i=1}^{n} |z_i|^2} \tag{20}$$

where $\|\cdot\|_2$ is the usual Euclidean norm.

Minimization of the functional $\phi(z)$ is equivalent to minimization of:

$$\psi(z) = \sum_{i=1}^{n} \left( \sum_{j=1}^{n} a_{ij} z_j - t_i \right) \left( \sum_{j=1}^{n} \bar{a}_{ij} \bar{z}_j - \bar{t}_i \right) + \sigma \sum_{i=1}^{n} z_i \bar{z}_i \tag{21}$$

where bars indicate complex conjugation.

Differentiating with respect to the components of $z$ we find that the minimum is obtained as the solution of the linear system (starred quantities denote adjoint matrices)

$$(\sigma I + A^* A) z = A^* t. \tag{22}$$

Green's function for equation (9) is (see Appendix A),

$$G_0(|r - \rho|) = \tfrac{1}{4} i H_0^2(e^{i\pi/4} k_0 |r - \rho|) \tag{23}$$

where $H_0^2$ is the Hankel function of the second kind of order 0.

The fact that in equation (23) we have a complex argument which has small absolute value (because of small thermal wavenumbers) is the main cause for the ill-posedness of the linear system. In contrast, optical and acoustic tomographic systems are not ill-posed, due to the fact that the magnitudes of the relevant wavenumbers are large (several orders of magnitude larger than the thermal wave-numbers). $H_0^2$ has an essential singularity at the origin causing uncontrolled behaviour of the function when the argument is small ($\ll 1$). This, in turn, causes the matrix of coefficients $A_{km}$ to be ill-behaved.

The initial field $T_i$, which is the solution of

$$(\nabla^2 + \tilde{k}_0^2) T(r) = 0 \tag{26}$$

is (see appendix B)

$$T_i(r) = H_{1/2}^2(\tilde{k}_0 r)/\sqrt{r}. \tag{27}$$

$H_{1/2}^2$ is the Hankel function of the second kind of order 1/2.

## 4. Simulated tomographic inversions

Figures 2–4 illustrate results of a theoretical simulation, where we assumed a hole of diameter 0.5 mm and a plane thermal wave oscillating with frequencies 10 Hz, 50 Hz, 1000 Hz, respectively. An object function was constructed using equation (3), and assuming $F(r) = 1$ over the hole. We used a small grid of $8 \times 8$ points. We used equation (14) to calculate the scattered field and then solved equation (22) with regularization parameter $\sigma = 10^{-8}$ to reconstruct the non-dimensional object function $(\nu^2(r) - 1)$. This value of $\sigma$ was chosen so as to yield optimum quality reconstructions. A more detailed discussion of the general criteria established for the

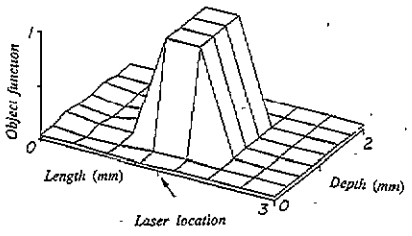


**Figure 2.** Wave reconstruction of theoretical object function. The intensity modulation frequency of the exiting laser is 10 Hz.

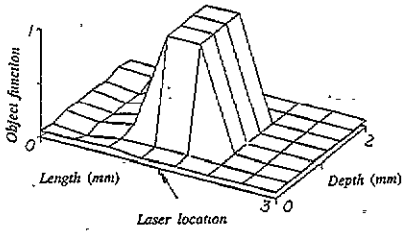


**Figure 3.** Wave reconstruction of theoretical object function. The intensity modulation frequency of the exciting laser is 50 Hz.

choice of optimal $\sigma$ values and of the discretization interval with respect to defect geometry has been presented elsewhere [17]. The value of the thermal diffusivity used for the material region surrounding the air gap ('hole') was $\alpha(r) = 0.9\,\mathrm{cm^2\,s^{-1}}$, well within the range of values characteristic of aluminium [11].

We observe excellent reconstruction for the low frequencies, figures 2–3, and good reconstruction for the high frequency tomography, figure 4. Note that the reconstruction is very good despite the small grid (which is the reason why the circular nature of the hole is not apparent), and the very wide range of assumed laser beam intensity modulation frequencies.

The success of these reconstructions attests to the satisfactory performance of the Born approximation. This is also expected theoretically, since the condition for the validity of the Born approximation (in freely propagating fields) is that the scattered field be smaller than the incident field [9]. This is certainly the case with the very rapidly spatially decaying thermal-wave field, although no formal proof of the extension of the validity of the above condition to the thermal-wave case has been constructed. This rapid spatial decay of the pseudo-propagating subsurface thermal-wave field is further responsible for the absence of multiple scattering of thermal waves, especially at higher modulation (and spatial) frequencies, where the attenuation is stronger. This is a remarkable advantage of the thermal-wave tomography over other tomographies based on freely propagating fields and holds the promise of high fidelity reconstructions from materials which are normally efficient scatterers of acoustic or optical waves (e.g. composites, macromolecular and polymeric solids etc).

## 5. Experimental results

An aluminium sample the dimensions of which were 3.75 mm wide and 2 mm thick was illuminated on one side with a focused laser beam at various points and a

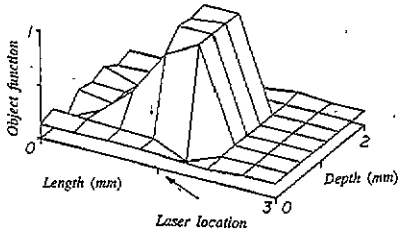


**Figure 4.** Wave reconstruction of theoretical object function. The intensity modulation frequency of the exciting laser is 1000 Hz.

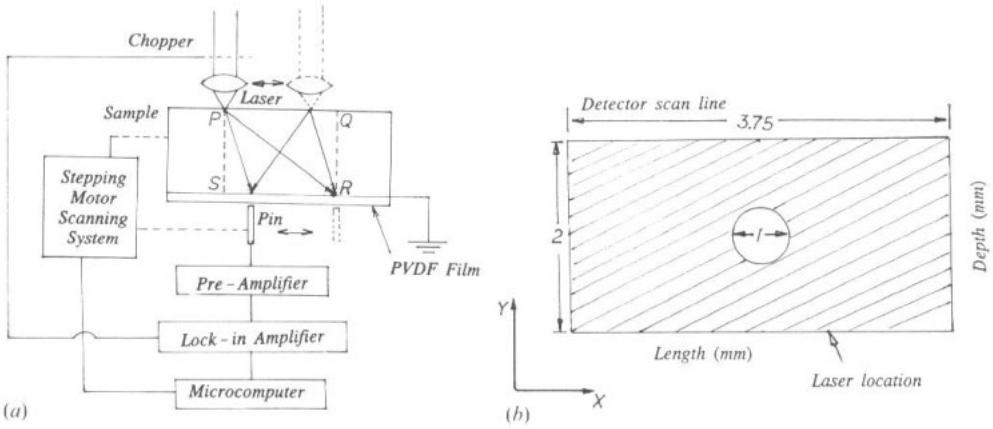


**Figure 5.** (*a*) Cross section of the experimental set-up, showing the lines joining two laser-pin scanning positions and the detection electronics. Laser intensity chopping frequency: 16 Hz. (*b*) Schematic description of sample and 2D coordinate system.

photopyroelectric pin detector was scanned along the other side. Details of the experimental set-up are shown in figure 5(*a*) [5]. In this experiment, the lock-in amplifier provides the amplitude and phase components of the steady-state thermal-wave field $T(r,\omega)$. With the present sample thickness, a contribution from twice-reflected thermal waves might be expected at $f = 16$ Hz modulation, corresponding to one reflection at the back surface of the sample followed by one more reflection at the front surface. The magnitude of such an added contribution to the thermal-wave field generated from the first transmission at the back would be decreased by a factor [18]

$$R \sim \left(\frac{1-b}{1+b}\right)e^{-2k_0 l} \approx 0.97\,e^{-2\times 11.07\times 0.2} = 1.15\times 10^{-2} \tag{26}$$

where $l$ is the aluminium thickness and

$$b \equiv \frac{k_{\mathrm{PVDF}}\sqrt{\alpha_{\mathrm{Al}}}}{k_{\mathrm{Al}}\sqrt{\alpha_{\mathrm{PVDF}}}}$$

is an interfacial thermal-wave reflection coefficient, with [18]

$$k_{\mathrm{Al}} = 2.008\times 10^{2}\,\mathrm{W\,mK^{-1}} \qquad \alpha_{\mathrm{Al}} = 8.2\times 10^{-5}\,\mathrm{m^2\,s^{-1}}$$

$$k_{\mathrm{PVDF}} = 0.13\,\mathrm{W\,mK^{-1}} \qquad \alpha_{\mathrm{PVDF}} = 5.4\times 10^{-8}\,\mathrm{m^2\,s^{-1}}.$$

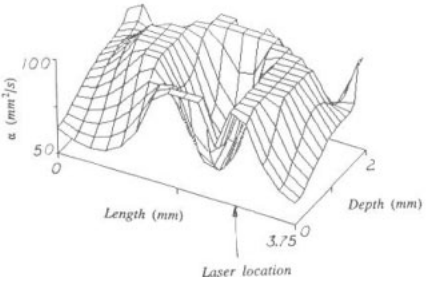


**Figure 6.** Ray optic reconstruction of thermal diffusivity; hole at the centre of the sample cross section.

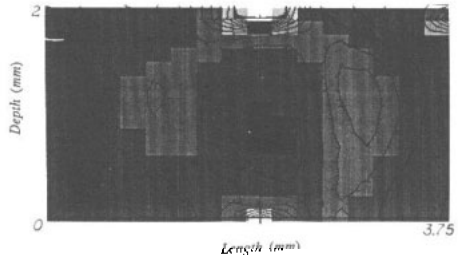


**Figure 7.** Isometric contour lines of thermal diffusivity tomogram, from ray optic reconstruction.

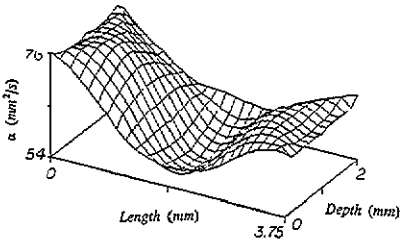


**Figure 8.** Wave tomographic reconstruction of thermal diffusivity; hole at the centre of the sample cross section.

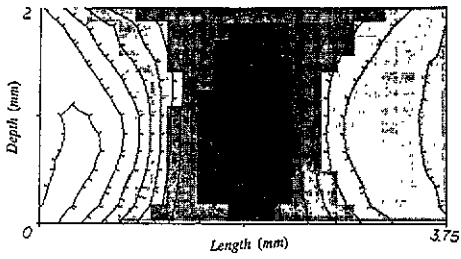


**Figure 9.** Isometric contour lines of thermal diffusivity tomogram, from wave optic reconstruction.

From the small magnitude of the correction term, equation (26), it was concluded that such a reflected thermal-wave contribution to our tomographic reconstruction was essentially negligible. The sample had a machined hole in its middle with diameter of 1 mm (figure 5(*b*)). Two dimensional reconstruction was carried out [5] using multiplexing all the laser and detector positions (figure 5(*b*)). The results of the ray optic reconstruction [5] from the transmitted thermal-wave amplitude and phase are presented in figure 6 (thermal diffusivity), and in figure 7 (isometric contour lines). The location of the hole in the $x$ direction is good, however, the depth is somewhat smeared out and distorted, while the defect size is underestimated. The ray optic reconstruction was performed using 26 detector positions for every one of the 26 laser positions. In figure 6 (and subsequently in figures 8, 10, 12 and 13), owing to the thinness of the sample and for clarity, a 13-point resolution is shown along the depth ($y$) coordinate, each point corresponding to an averaging interpolation between three adjacent data points.

In all the wave reconstruction results presented here we used both the amplitude and the phase of the scattered field. This was done by solving the linear system (22) over the complex field. The solution of the system, the object function, should be real, and the result of the computation was very nearly so (the imaginary part was less than 10% of the absolute value).

Figure 8 describes the reconstruction by the current method, using only one laser position and 26 detector positions. We note a more accurate location of the hole in both directions than in figure 6, along with a much more realistic size and shape of the defect. In figure 9 we present the contour lines. In this experiment, and in all subsequent experiments in which the slice tomograms were reconstructed with the

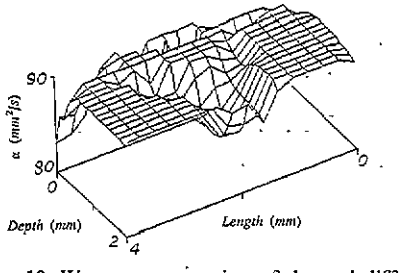


**Figure 10.** Wave reconstruction of thermal diffusivity; hole at the edge of the sample.

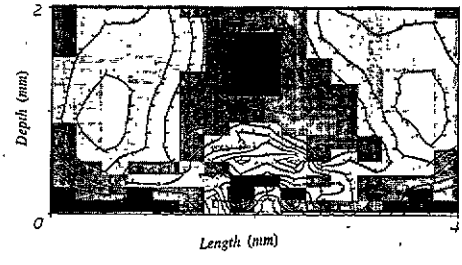


**Figure 11.** Isometric contour lines of thermal diffusivity, from wave reconstruction; hole at the edge of the sample.

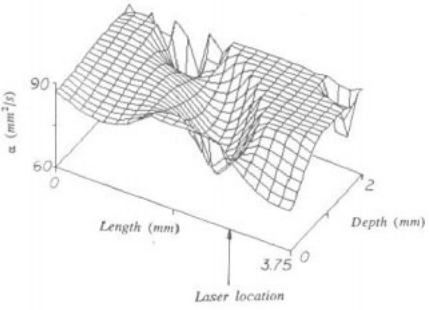


**Figure 12.** Wave reconstruction of thermal diffusivity; fine computational grid, laser at 2.4 mm from the left edge.

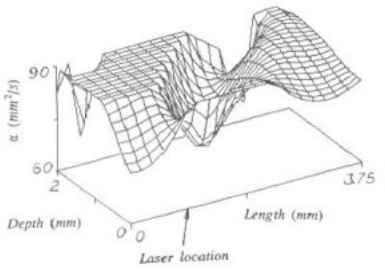


**Figure 13.** Wave reconstruction of thermal diffusivity; fine computational grid, laser at 1.3 mm from the right edge.

methodology presented in this paper, the scattered field was measured on 26 points. Then the data were interpolated to the desirable number of points, so that the number of resulting equation was the same as the number of unknowns. The interpolation method used was cubic splines. In figures 8 and 9 we also observe some edge effects (artifacts). Figures 10 and 11 describe similar results, only this time the hole was moved to the lower edge of the sample. The actual location of the hole is marked with H on figure 11. We note here, again, good reconstruction of the hole position in the $x$ and $y$ directions. Similar reconstructions using the ray optic approach resulted earlier [5] in locating the defect, but the defect presence was much less noticeable than in figures 10 and 11.

Figure 12 is similar to figure 8 only this time we used a finer computational grid. We find that we have a well resolved shape contour of the edge of the hole on the side of the laser location. In figure 13 the laser was moved to a different location on the other side of the hole, and again we see a clear, well resolved shape contour of the edge of the hole on the laser side. Therefore, it may be concluded that the use of higher resolution delineates accurately the actual contour of the hole on the side close to the position of the laser. It can further be seen from the inspection of figures 12 and 13 that a combination of the two laser positions may be able to delineate the entire contour image of the subsurface wall.

## 6. Conclusions

A rigorous matrix-equation-based wave approach to the thermal-wave slice inverse tomographic problem was presented, along with a combined computational–analytical implementation on metallic samples with well characterized sub-surface defects. Reconstructions of photopyroelectric thermal diffusivity tomograms showed that for a good quality and accurate reconstruction we need to use two or three laser locations, and perhaps repeat the process by reversing the detector and laser positions. These operations are currently under investigation.

The new method yields superior reconstructions to those originally obtained by ray optic approximations, and is capable of solving the Helmholtz pseudowave equation and reconstructing the diffusivity field.

**Acknowledgments**

The authors wish to acknowledge the support of the Natural Sciences and Engineering Research Council of Canada (NSERC), and Rafael for a sabbatical research leave (OP) which made this work possible.

## Appendix A. Integral-representation of the two-dimensional themal-wave Green function

Following Mandelis [4] we find that the Green function for the two dimensional thermal-wave Helmholtz equation should be

$$G_0(r|\rho) = \frac{1}{4\pi^2}\int_{\alpha-i\infty}^{\alpha+i\infty} \exp[\tilde{k}_\alpha^2(x-\xi)]\,d\tilde{k}_\alpha \int_{\beta-i\infty}^{\beta+i\infty} \frac{\exp[\tilde{k}_\beta(y-\eta)]}{\tilde{k}_\beta^2 - (\tilde{k}_0^2 - \tilde{k}_\alpha^2)}\,d\tilde{k}_\beta \tag{A.1}$$

Using the theorem of residues [19] we obtain

$$G_0 = \frac{-i}{4\pi}\int_{\alpha=i\infty}^{\alpha+i\infty} \frac{\exp[\tilde{k}_\alpha X - \sqrt{\tilde{k}_0^2 - \tilde{k}_\alpha^2}\,Y]}{\sqrt{\tilde{k}_0^2 - \tilde{k}_\alpha^2}}\,d\tilde{k}_\alpha \tag{A.2}$$

where $X = x - \xi$ and $Y = y - \eta$.

Define, $\tilde{k}_\alpha = \tilde{k}_0\cos(\theta - \phi)$ and $\tan\phi = Y/X$. Then

$$\begin{aligned}\tilde{k}_\alpha X - \sqrt{\tilde{k}_0^2 - \tilde{k}_\alpha^2}\,Y &= \tilde{k}_0[X\cos(\theta-\varphi) - Y\sin(\theta-\varphi)] \\ &= \tilde{k}_0\cos\theta\frac{X}{\cos\varphi} = \tilde{k}_0 R\cos\theta\end{aligned} \tag{A.3}$$

The path of integration to ensure convergence is along $\alpha = \pi/2$, so that

$$G_0 = \frac{i}{4\pi}\int_{\pi/2-i\infty}^{\pi/2+i\infty} \exp(\tilde{k}_0 R\cos\theta)\,d\theta \tag{A.4}$$

Changing variable: $\theta = -iu$

$$\int_{\pi/2-i\infty}^{\pi/2+i\infty} \exp(\tilde{k}_0 R\cos\theta)\,d\theta = i\int_{-\infty-\pi i/2}^{\infty+\pi i/2} \exp(\tilde{k}_0 R\cosh u)\,du. \tag{A.5}$$

Let $u = v + 3\pi i/2$; then $\cosh u = i\sinh v$ and

$$\begin{aligned}\int_{-\infty-\pi i/2}^{\infty+i/2} \exp(\tilde{k}_0 R\cosh u)\,du &= \int_{-\infty-2\pi i}^{\infty-\pi i} \exp(i\tilde{k}_0 R\sinh v)\,dv \\ &= \int_{-\infty}^{\infty-\pi i} \exp(i\tilde{k}_0 R\sinh v)\,dv\end{aligned} \tag{A.6}$$

The right hand side of (A.6) follows from the fact that the hyperbolic functions are $2\pi i$ periodic.

It follows from equations (A.4) and (A.6) that [20]

$$G_0(R) = \tfrac{1}{4}iH_0^2(e^{i\pi/4}k_0R) \tag{A.7}$$

where $H_0^2$ is the Hankel function of the second kind of order 0.

## Appendix B. Solution of the homogeneous Helmholtz pseudowave equation

In the experimental configuration of figure 1 we have a point source at the surface, generating thermal waves. If we assume a homogeneous medium, then the thermal wave propagation will be similar to a spherical wave. Let the angle $\theta$ be defined in a plane perpendicular to the plane of the crossed-sectional slice in figure 1. Assuming symmetry in $\theta$ (i.e. invariability of material and scattering object geometries and thermophysical properties in the direction perpendicular to the slice plane), we obtain the equation

$$(\nabla^2 + \tilde{k}_0^2)T(r) = 0 \tag{B.1}$$

In spherical coordinates,

$$\frac{\partial}{\partial r}\left(r^2\frac{\partial T}{\partial r}\right) + \frac{1}{\sin\varphi}\frac{\partial}{\partial\varphi}\left(\sin\varphi\frac{\partial T}{\partial\varphi}\right) + \tilde{k}_0^2 r^2 T = 0. \tag{B.2}$$

Assuming $T(r,\varphi) = u(r)v(\phi)$, we obtain the following two ordinary differential equations by separation of variables:

$$\frac{1}{u}\frac{\mathrm{d}}{\mathrm{d}r}\left(r^2\frac{\mathrm{d}u}{\mathrm{d}r}\right) + \tilde{k}_0^2 r^2 = -\eta \tag{B.3}$$

and

$$\frac{1}{v\sin\varphi}\frac{\mathrm{d}}{\mathrm{d}\varphi}\left(\sin\varphi\frac{\mathrm{d}v}{\mathrm{d}\varphi}\right) = \eta. \tag{B.4}$$

Substituting $\omega = \cos\phi$ in equation (B.4), we obtain,

$$(1-\omega^2)\frac{\mathrm{d}^2v}{\mathrm{d}\omega^2} - 2\omega\frac{\mathrm{d}v}{\mathrm{d}\omega} + \lambda(\lambda+1)v = 0 \tag{B.5}$$

where $\eta = \lambda(\lambda+1)$.

Equation (B.3) can be written as,

$$r^2\frac{\mathrm{d}^2u}{\mathrm{d}r^2} + 2r\frac{\mathrm{d}u}{\mathrm{d}r} + (\tilde{k}_0^2 r^2 - \eta)u = 0. \tag{B.6}$$

Substituting in equation (B.5) $z = \tilde{k}_0 r$ and $u(r) = r^{-1/2}w(z)$, we obtain,

$$z^2\frac{\mathrm{d}^2w}{\mathrm{d}z^2} + z\frac{\mathrm{d}w}{\mathrm{d}z} + [z^2 + (\eta - \tfrac{1}{4})] = 0 \tag{B.7}$$

Equation (B.5) is a Legendre equation [20], and equation (B.7) is a Bessel equation [19]. Choosing $\lambda = 0$ in equation (B.4) results in $v \equiv 1$, and from equation (B.7) we conclude that $w(z)$ must be a Bessel function of order $v = \frac{1}{2}$. The Bessel function whose behaviour

is $O(1/r)$ for both small and large values of $r$ and is most suitable for experimental results was found to be

$$w(z) = H_{1/2}^2(z) \tag{B.8}$$

and hence we can write

$$T(r,\varphi) = T(r) = H_{1/2}^2(\tilde{k}_0 r)/\sqrt{r} \tag{B.9}$$

where $H_{1/2}^2$ is the Hankel function of the second kind of order $\frac{1}{2}$.

## References


[1] Iravani M V and Wickramasinghe H K 1985 Scattering matrix approach to thermal wave propagation in layered structures *J. Appl. Phys.* **58** 122

[2] Iravani M V and Nikoonahad M 1987 Photothermal waves in anisotropic media *J. Appl. Phys.* **62** 4065

[3] Mandelis A 1989 Theory of photothermal wave diffraction and interference in condensed media *J. Opt. Soc. Am.* A **6** 298

[4] Mandelis A 1991 Theory of photothermal wave diffraction tomography via spatial Laplace spectral decomposition *J. Phys. A Math. Gen.* **24** 2485

[5] Munidasa M and Mandelis A 1991 Photopyroelectric thermal wave tomography of almuminium with ray optic reconstruction *J. Opt. Soc. Am.* A **8** 1851

[6] Munidasa M, Mandelis A and Ferguson C 1992 'Resolution of photothermal imaging of subsurface defects in metals, with ray optic reconstruction *Appl. Phys.* A **54** 244

[7] Favro L D, Kuo P K and Thomas R L 1993 Real time thermal wave imaging in *Non-destructive Evaluation (Principles & Perspectives of Photothermal & Photoacoustic Phenomena* Vol II) ed A Mandelis, (Englewood Cliffs, NJ: Prentice Hall) p 24

[8] Busse G and Walther H G 1992 Photothermal nondestructive evaluation of materials with thermal waves *Principles & Perspectives of Photothermal & Photoacoustic Phenomena* Vol I, ed A Mandelis (New York: Elsevier) p 207

[9] Kak A C and Slaney M 1988 *Principles of Computerized Tomographic Imaging* (New York: IEEE)

[10] Uejima A, Itoga F and Sugitani Y 1986 Non-destructive analysis of layered materials by depth resolved photoacoustic imaging *Anal. Sci.* **2** 113

[11] Touloukian Y S, Powell R W, Ho C Y and Nicolaou M C 1973 *Thermal Diffusivity* (New York: IFI/Plenum)

[12] Morse P M and Feshbach H 1953 *Methods of Theoretical Physics* (New York: McGraw-Hill) Ch 7

[13] Nahamoo D, Pan S X and Kak A C 1984 Synthetic aperture diffraction tomography and its interpolation-free computer implementation *IEEE Trans. Sonics Ultraonics* **SU-31** 218

[14] Hämmerlin G and Hoffman K H 1991 *Numerical Mathematics* (New York: Springer)

[15] Kress R 1989 *Linear Integral Equations* (New York: Springer)

[16] Hofmann B 1986 *Regularization for Applied Inverse and Ill-Posed Problems* (Leipzig: Teubner)

[17] Padé O and Mandelis A 1993 Computational thermal-wave slice tomography with back-propagation and transmission reconstructions *Rev. Sci. Instrum.* in press

[18] Mandelis A and Leung K F 1991 Photothermal-wave diffraction and interference in condensed media: experimental evidence in aluminum *J. Opt. Soc. Am.* A **8** 186

[19] Whittaker E T and Watson G N 1948 *A Course in Modern Analysis* (Cambridge: Cambridge University Press)

[20] Abramowitz M and Stegun I 1972 *Handbook of Mathematical Functioons* (New York: Dover)